ACS APPLIED MATERIALS & INTERFACES

Research Article

www.acsami.org

Enhanced Electrode Performance of Fe_2O_3 Nanoparticle-Decorated Nanomesh Graphene As Anodes for Lithium-Ion Batteries

Xiao Zhu,† Xinyu Song,† Xinlong Ma, and Guoqing Ning*

State Key Laboratory of Heavy Oil Processing, China University of Petroleum, Beijing, Changping 102249, P. R. China

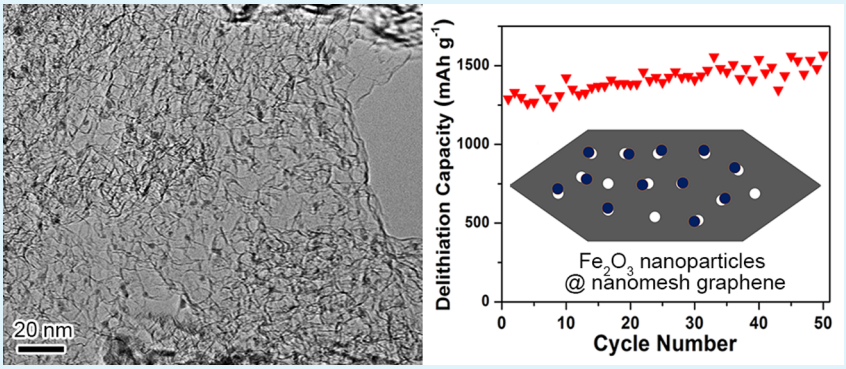

ABSTRACT: Nanostructured Fe_2O_3-nanomesh graphene (NMG) composites containing ~3 nm Fe_2O_3 nanoparticles (NPs) uniformly distributed in the nanopores of NMG are synthesized by an adsorption−precipitation process. As anodes for Li ion batteries (LIBs), the 10%Fe_2O_3−NMG composite exhibits an upward trend in the capacity and delivers a reversible specific capacity of 1567 mA h g^{-1} after 50 cycles at 150 mA g^{-1}, and 883 mA h g^{-1} after 100 cycles at 1000 mA g^{-1}, much higher than the corresponding values for the NMG electrode. The significant capacity enhancement of the 10%Fe-NMG composite is attributed to the positive synergistic effect between NMG and Fe_2O_3 NPs due to the catalytic activity of Fe_2O_3 NPs for decomposition of the solid electrolyte interface film. Our results indicate that decoration of ultrasmall Fe_2O_3 NPs can significantly change the surface condition of graphene. This synthesis strategy is simple, effective, and broadly applicable for constructing other electrode materials for LIBs.

KEYWORDS: *iron oxide, nanomesh graphene, composite, synergistic effect, catalytic activity, electrochemistry, lithium batteries*

1. INTRODUCTION

Rechargeable Li-ion batteries (LIBs) are currently the dominant power source for portable electronic devices. Although such batteries have gained commercial success, they are hampered in the increasing applications such as electric vehicles and power grids due to low energy capacity, insufficient power rates, and limited cycling stability.[1,2] Accordingly, extensive efforts have been devoted to developing new high-performance electrode materials for next-generation LIBs, such as low-dimension redox-active metal oxides.[3−6] Despite significant progress, the oxide anodes cannot harvest ideal performance because of their low conductivity characteristics and large volume changes during repeated charge/discharge.[7] To solve the challenges, making composites of low-dimension oxides and conductive carbons has therefore emerged as a most effective method toward high-performance anode materials.[8,9] To date, the composites are commonly prepared by simple coating of pyrolytic carbon species on nanoscale oxides, within active particles embedded in a conductive carbon.[10,11] However, the pyrolytic carbon cannot provide effective structure for strain and large volume expansion, thus offering only limited stability.

Alternatively, creating composites with porous characteristics has been proposed to overcome those limitations.[12−15] Such composites can be achieved by two categories: one is preparing the hybrid composites;[13] the other is building nanostructured composites.[15] Although these composites possess diverse structural characteristics, a common fundamental challenge is to improve electron and ion transport. In the first category of hybrid composites, graphene-oxide composites can be prepared via reduction of graphene oxide. The electron and ion transport pathways are formed by random growing oxides on reduced graphene sheets, which is poorly controlled and ineffective.[16,17] For better control, the second category of nanostructured composites are developed with active oxides integrated into three-dimensional graphene networks, and show much improved performance.[18−20] The development of oxide-based active materials from carbon coated oxides, hybrid composites to more advanced nanostructured composites leads to the combination of oxides with carbon materials toward success.[21] However, despite the extensive efforts, designing more effective material nanostructures for high-performance anode materials remains crucial and challenging.

Received: January 16, 2014
Accepted: May 2, 2014
Published: May 2, 2014

Recently, we have fabricated nanomesh graphene (NMG) using a chemical vapor deposition method, which is mainly composed of porous graphene of one to two layers and has a specific surface area (SSA) up to 2038 $m^2 g^{-1}$.[22] Herein, we reported an adsorption-precipitation process to fabricate a class of new composite architecture consisting of oxide materials assembled in such porous graphene for high-performance anode materials. Iron sesquioxide (Fe_2O_3) was used as model materials due to its high theoretical capacity (1005 mA h g^{-1} for Fe_2O_3, almost three times of graphite) and low cost.[23] Figure 1 outlines

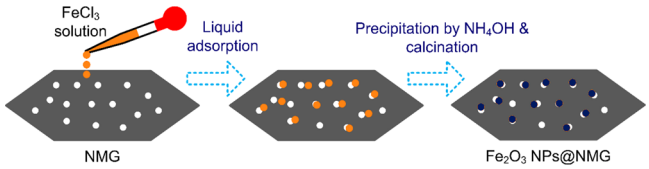

Figure 1. Schematic synthesis of Fe_2O_3–NMG composites.

the approach and structure of such composite. Firstly, based on the good absorbability of NMG, $FeCl_3$ aqueous solution was uniformly adsorbed into the porous structure of NMG. Subsequent dropwise adding $NH_3{\cdot}H_2O$ aqueous solution into the suspension leaded to the formation of $Fe(OH)_3$-NMG composite precursors. After following calcination of collected composite precursors, Fe_2O_3–NMG composites were available with Fe_2O_3 nanoparticles assembled into pores of NMG. With changing the concentration of $FeCl_3$ solution, the composition can be readily tuned for designed Fe_2O_3–NMG composites. Such unique composite structure has following features: (i) CVD-based graphene has high conductivity for electron transport; (ii) interconnected electrolyte-filled pore networks, (iii) large specific surface areas, and (iv) short ion diffusion lengths of low dimensional Fe_2O_3 nanoparticles allow rapid ion transport. Moreover, the porous structure endows such composites with elastic deformation to retain the structure integrity during battery reactions.

In light of recent advances in the synthesis of controlled composite materials, this strategy provides a general fabrication approach toward metal oxide-based high-performance anode materials. Note that reduced graphene can be easily loaded active particles for energy storage and other applications; however, such graphene exhibits rather low conductivity compared to CVD-grown graphene.[22,24] Similarly, almost all CVD-based planar graphene has strong hydrophobic properties and aggregates easily in use.[25] By comparison, the nanomesh structure of NMG acts as nanoscale vessels to load a huge family of compounds, offering an important platform for preparing advanced materials. In this case, the metal oxide nanoparticles (NPs) are not used to separate graphene sheets, but to change the surface condition of graphene, which is crucial to many applications. However, to date, no work on this point has been reported. This work provides a simple but efficient fabrication strategy toward new nanostructured composites by loading ultrasmall particles into high-quality NMG.

2. EXPERIMENTAL SECTION

NMG was synthesized using a reported chemical vapor deposition method.[22] A freeze drying was performed to maintain the porous structure. In a typical synthesis of 10%Fe_2O_3–NMG composite, 0.5 g of NMG was dispersed into 300 mL of alcohol-water (1:2, v/v) solution by sonication for 0.5 h. Then, $FeCl_3$ solution (0.007 mol L^{-1}, 100 mL) was added into the NMG suspension under stirring for 0.5 h. After that, excess ammonia solution ($NH_3{\cdot}H_2O$, 25 wt %) was added dropwise with stirring for 2 h. The obtained $Fe(OH)_3$-NMG composite precursor was collected and dried in air at 100 °C. Finally, the $Fe(OH)_3$-NMG was obtained after calcinating at 450 °C in Ar for 1 h. By changing $FeCl_3$ concentration, 20%Fe-NMG and 70%Fe-NMG were prepared using the same method. For comparison, pure Fe_2O_3 particles were prepared without the presence of NMG, and a physical mixture of 10 wt % pure Fe_2O_3 particles and 90 wt % NMG (10%Fe_2O_3 + 90%NMG) was also prepared.

The as-prepared samples were characterized by transmission electron microscope (TEM, JEM 2010 microscope, operated at 120.0 kV), scanning transmission electron microscope (STEM, FEI, Tecnai G^2 F20) equipped with energy dispersive spectrometer (EDS), X-ray photoelectron spectrometer (XPS, PHI700) and X-ray diffraction (XRD, D/max 2400 with Cu Kα radiation). TGA was performed on a Q500 at a heating rate of 10 or 20 °C/min in air flow. The pore size

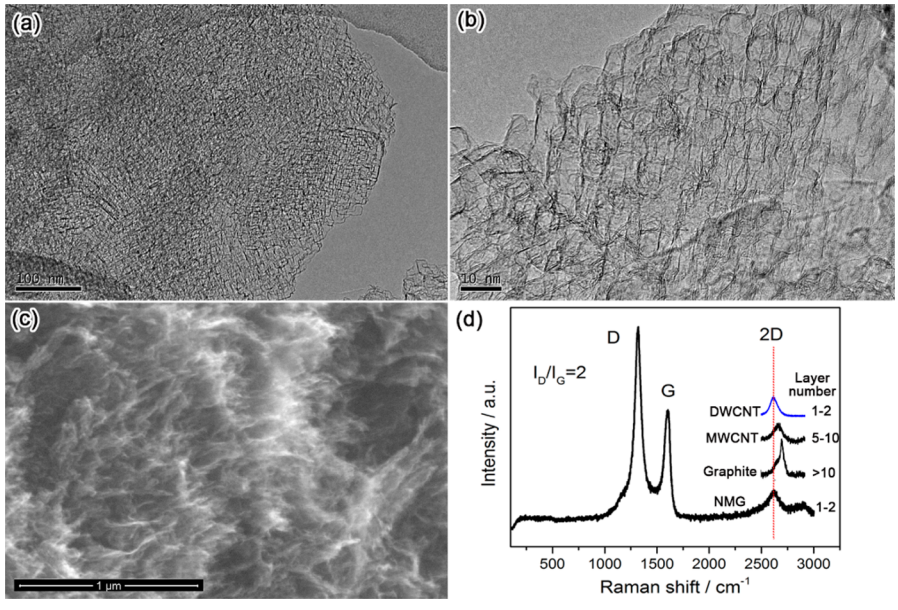

Figure 2. (a, b) TEM images, (c) SEM image, and (d) Raman spectrum of NMG.

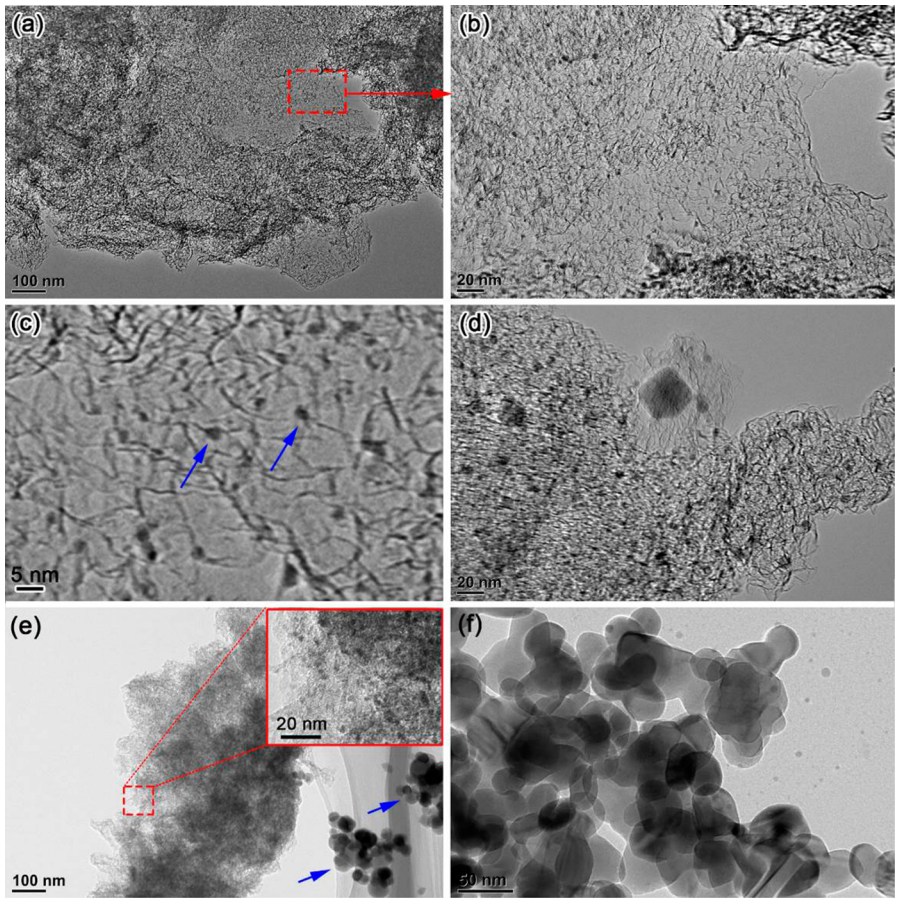

Figure 3. (a–c) TEM images of 10%Fe-NMG, (d) 20%Fe-NMG, (e) 70%Fe-NMG, and (f) pure Fe_2O_3. The inset of e shows high-magnification TEM image of 70%Fe-NMG composite.

distribution was measured on Micrometritics ASAP 2010 using nitrogen as adsorptive.

Electrochemical measurements were performed using half-coin cells. The working electrodes consisted of 80 wt % composite material, 5 wt % acetylene black (Super-P), and 15 wt % polyvinylidene fluoride binder. Lithium metal was used as the counter/reference electrode. Celgard 2400 membrane was used as separator. The electrolyte was a solution of 1 M $LiPF_6$ in ethylene carbonate/dimethyl carbonate (1:1 by volume). Cyclic voltammetry (CV) measurements were carried out on a CHI 660D electrochemical workstation at a scan rate of 0.1 mV s^{-1}. Alternating current (AC) impedance spectra were measured in the frequency range from 0.01 to 100000 Hz. Data fitting of the AC impedance spectra was performed by Zview software. The cells were discharged and charged from 0.01 to 3.0 V using a charge–discharge tester at room temperature.

3. RESULTS AND DISCUSSION

Figure 2 a and b show the representative transmission electron microscopic (TEM) morphology of NMG, which is composed of only one to two graphene layers. It has abundant nanopores and surface corrugations, which helps to avoid agglomeration of graphene sheets. SEM observation also presents a fluffy appearance with loose stacking (Figure 2c), which favors adsorption of precursor solution. Raman spectrum of NMG (Figure 2d) has a strong D band, with a D to G intensity ratio (I_D/I_G) of 2, which could be ascribed to the edges of the nanomesh structure. The 2D peak position of NMG (2616 cm^{-1}) is similar to that of double-walled carbon nanotubes (DWCNTs, 2610 cm^{-1}) and is obviously downshifted as compared to those of multi-walled carbon nanotubes (MWCNTs, 2658 cm^{-1}) and graphite (2685 cm^{-1}). It indicates that the NMG is mainly composed of one to two graphene layers, well-consistent with the TEM observation of Figure 2b. It has been found that Raman spectrum of graphene with one or two layers is different from that with more than 5 layers by the lower frequency of the 2D band.[26] Therefore, the graphene layer number can be determined by comparing the 2D band position with single, double or multi-layered graphene. However, due to the easy agglomeration of graphene, a stable bulk material with single-layered graphene is almost not available. Hence, we suggest that carbon nanotubes (CNTs) with different wall numbers can be used as Raman calibration samples for determination of graphene layer number, because the selective synthesis of CNTs with single or double walls has been a mature technique.[27,28]

Figure 3 shows the TEM images of Fe_2O_3–NMG composites with different Fe_2O_3 loading. As observed, Fe_2O_3 NPs with size of 1.5–5 nm were uniformly distributed on NMG sheets in the 10% Fe-NMG composite (Figure 3a–c). The Fe_2O_3 NPs are attached on the walls of meshes (as indicated by the arrows in Figure 3c), forming a core@void@shell structure. The void accommodates volume changes during the reactions.[29] Formation of the core@void@shell structure is attributed to the unique adsorption-precipitation process. Once a drop of $FeCl_3$ solution enters a mesh pore, the fluidity of the adsorbed liquid drop is significantly reduced, which hinders the continuous growth of the precipitated nanoparticles. Compared to 10%Fe-NMG, Fe_2O_3 NPs with much larger particle size (up to 20–30 nm) are observed in 20%Fe-NMG composites (Figure 3d), indicating

that the increased amount of $FeCl_3$ has led to increased Fe_2O_3 particle sizes. In 70%Fe-NMG composites, individual Fe_2O_3 particle size reaches 20-100 nm (Figure 3e), suggesting high loading of Fe_2O_3 NPs (the inset of Figure 3e). It indicates that the precipitation of excessive Fe salt had taken place in the liquid phase rather than on the surface of NMG, which is crucial to the formation of a uniform composite. As a control sample, pure Fe_2O_3 particles prepared by a similar precipitation process have a particle size distribution from 30 to 50 nm (Figure 3f).

Figure 4 shows a dark field STEM image of the 10%Fe-NMG composite and its elemental mapping of C (red), O (brown) and

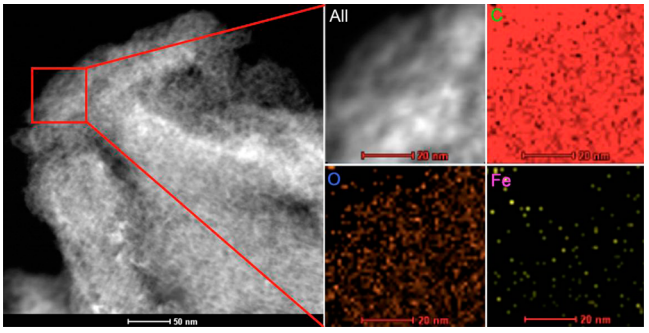

Figure 4. STEM image (left) and EDS elemental mapping (right) of 10%Fe-NMG.

Fe (yellow) that are obtained by energy dispersive X-ray spectroscopy (EDX). The bright dots in the Fe mapping correspond to the Fe_2O_3 NPs distributed on NMG. These results further confirm the embedment of Fe_2O_3 within NMG matrix, which suggest uniform dispersion of Fe_2O_3 NPs in the 10%Fe-NMG composite. Figure 5a presents HRTEM image of 10%Fe-

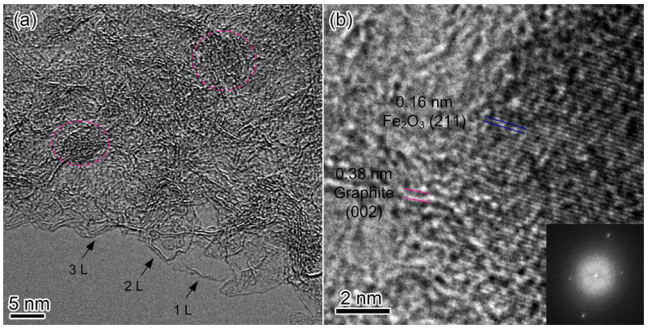

Figure 5. HRTEM images of 10%Fe-NMG. The inset of b shows the corresponding SAED pattern of the sample.

NMG to confirm the existence of Fe_2O_3 nanoparticles and disordered stacking of graphene with 1−3 layers. The oxide nanoparticles exhibit a lattice fringe 0.16 nm, which corresponds to the (211) planes of the Fe_2O_3 crystals. Graphene with (002) lattice plane around 0.38 nm was also observed around Fe_2O_3 nanoparticles, suggesting the intimate interfacial contacts. Figure 6a shows that Fe_2O_3 NPs in 10%Fe-NMG composite have a narrow size distribution from 1.5 to 5 nm with centralization at ∼3 nm. In contrast, the averaged pore size of pure NMG is ∼4 nm, slightly larger than that of Fe_2O_3 NPs. Thus, the size differences can provide space for expansion during Li insertion and extraction. The elemental composition of the Fe_2O_3−NMG composites was quantitatively confirmed by TGA (Figure 6b), which are well consistent with the values calculated from the proportion between NMG and Fe salts. To confirm the chemical composition of the as-prepared 10%Fe-NMG composite, XPS measurements were carried out in the region of 0-1200 eV (Figure 6c). The Fe 2p XPS spectra of the composite exhibits intensified peaks at 711.2 and 724.8 eV, both corresponding to the Fe^{3+} $2p_{2/3}$ spin-orbit peak of Fe_2O_3 (the inset of Figure 6c),[30] which confirms the existence of Fe_2O_3 in the composite. Figure 6d shows the XRD patterns of Fe_2O_3, NMG and 10%Fe-NMG composite. All the diffraction peaks of the pure Fe_2O_3 are in good agreement with the standard profiles of Fe_2O_3 (JCPDS No. 33-0664). No obvious diffraction peaks of the Fe_2O_3 can be observed in the XRD pattern of 10%Fe-NMG, indicating that the Fe_2O_3 NPs in the composite have been well dispersed on NMG without obvious agglomeration. The peak of the composite at 24.9° is much weaker than that of NMG, suggesting more disordered stacking of NMG in the composite.[31]

Lithium insertion and extraction curves of the 10%Fe-NMG composite for the 1st, 2nd, and 3rd cycles measured at the current density of 50 mA g^{-1} are shown in Figure 7a. In the first discharge curve, a plateau at 1.0 V (vs Li/Li^+) is clearly observed, which is related to decomposition of the electrolyte and formation of a solid-electrolyte interface (SEI) layer.[32] Subsequently, the plateau is not observed from the next cycle onward, indicating that formation of the SEI film complete in the first discharge cycle. The first reversible capacity of the 10%Fe-NMG composite is 1692 mA h g^{-1} at the current density of 50 mA g^{-1} and the capacity does not decrease through the subsequent discharge/charge cycles. The irreversible capacity loss in the first cycle can be attributed to the irreversible lithium consuming due to the formation of the SEI layer owing to the significant porous structure and large SSA of NMG.[33,34] The lithium insertion and extraction curves for 10%Fe-NMG are similar to those for NMG. The voltage plateaus at ∼1.6 and ∼0.8 V, resulting from the lithium reaction with Fe_2O_3 NPs,[33] are not clearly observed, probably because of the quite limited Fe_2O_3 content (12.4 wt %) of 10%Fe-NMG.

Figure 7b shows the rate capability of different materials. Although the initial capacity of the 10%Fe-NMG composite (1692 mA h g^{-1} at 50 mA g^{-1}) is less than that of NMG (2000 mA h g^{-1}), an upward tendency of the capacity is observed for 10%Fe-NMG, exhibiting higher capacities than the NMG in the following cycles. At the current density of 1000 mA g^{-1}, the delithiation capacity of 10%Fe-NMG retains ∼555 mA h g^{-1}, much higher than that of NMG (∼295 mA h g^{-1}) and Fe_2O_3 (∼295 mA h g^{-1}). Moreover, the Li storage capacity of 10%Fe-NMG keeps an upward trend during long term cycling at both low and high rate (Figure 7c, d), showing much better cycling stability as compared to 20%Fe-NMG, 70%Fe-NMG and pure Fe_2O_3. For example, the delithiation capacity of the 10%Fe-NMG composite increases from 1289 to 1567 mA h g^{-1} (21.6% enhancement, Figure 7c) at the current density of 150 mA g^{-1}. As a sharp contrast, the delithiation capacity of the 20%Fe-NMG composite decreases from 1180 to 1060 mA h g^{-1} after 50 cycles. When the current density increases to 1000 mA g^{-1}, the delithiation capacity of 10%Fe-NMG still keeps at a high level and gradually increases from 814 to 883 mA h g^{-1} after 100 cycles, much higher than the other materials (Figure 7d). While, there is a capacity degradation of 10%Fe-NMG composite in the first few cycles in Figure 7d, which ascribes to the high current density that can accelerate the formation of SEI films and the SEI films aren't stable at high current density, so the capacity decreases in the first few cycles. While along with the time, the activated Fe_2O_3 further inhibits and decomposes the formation

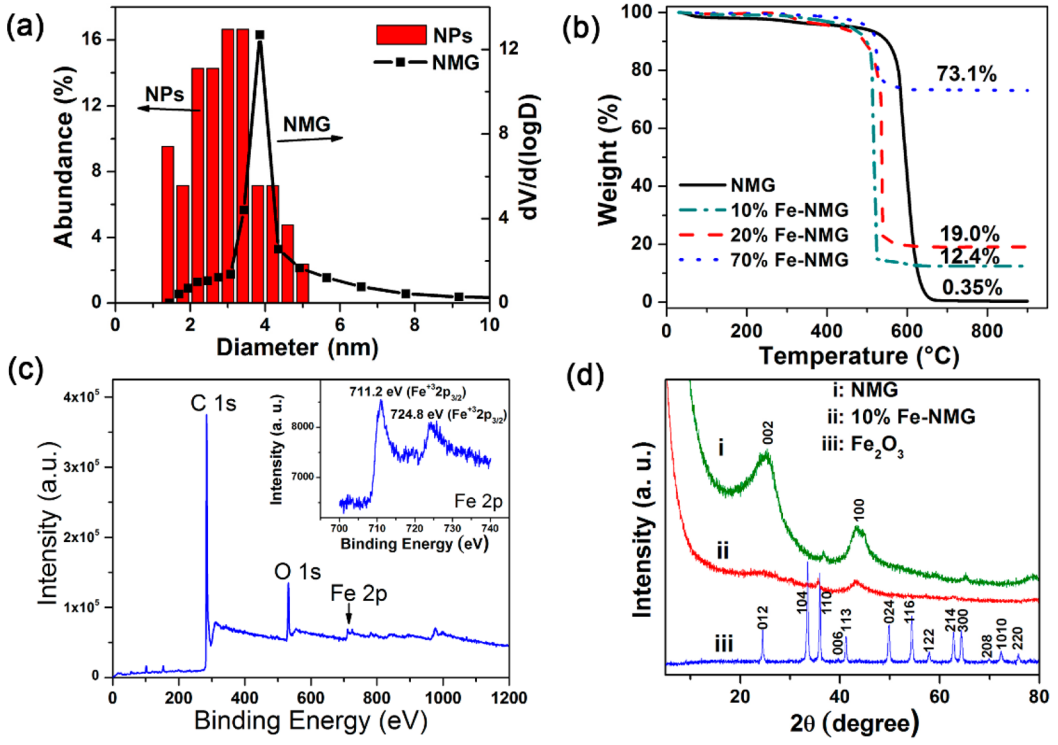

Figure 6. (a) Size distribution of Fe_2O_3 NPs in 10%Fe-NMG and the pore size distribution of NMG (*D* represents the pore diameter and *V* is the pore volume). (b) TGA curves of NMG and Fe_2O_3−NMG composites. (c) XPS survey spectrum and Fe 2p spectrum (inset) of 10%Fe-NMG. (d) XRD profiles of Fe_2O_3, NMG, and 10%Fe-NMG.

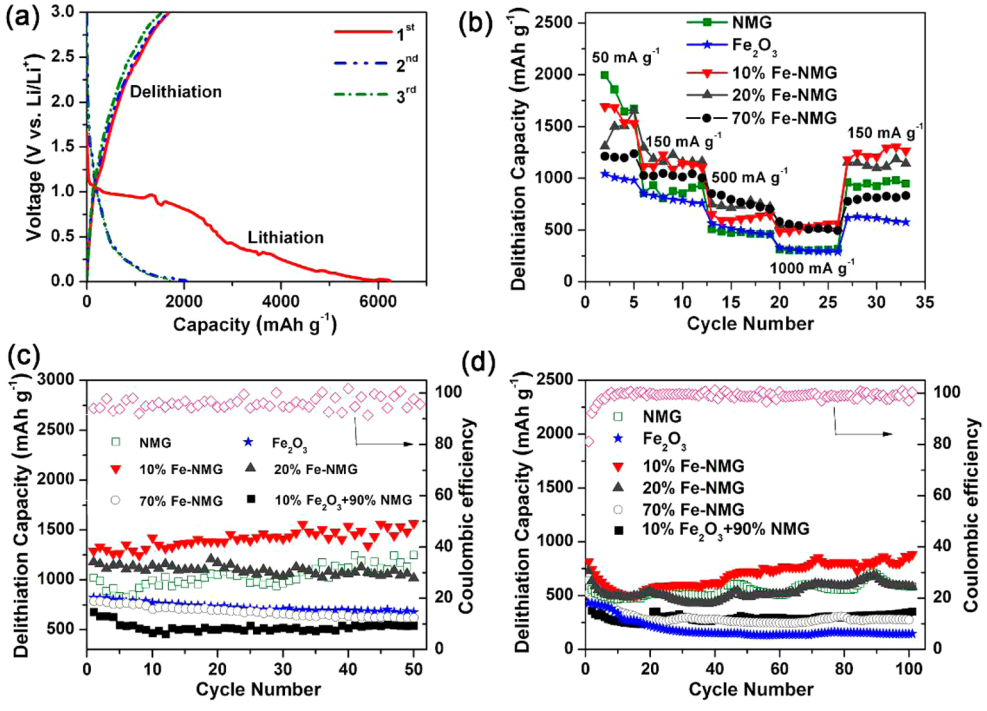

Figure 7. (a) Lithium insertion and extraction curves of the 10%Fe-NMG composite cycled between 3 and 0.01 V (vs. Li^+/Li) at the current density of 50 mA g^{-1}. (b) Rate capability and (c, d) cycling stability at the current density of 150 mA g^{-1} and 1000 mA g^{-1} for as-prepared materials. The pink data in c and d represent the Coulombic efficiency of the 10%Fe-NMG during the cycling process.

of SEI films, so the capacity increases afterward (The first Coulombic efficiency of 10%Fe-NMG is only ~83%, then it increases afterward). For comparison, the cyclability data of the physical mixture 10%Fe_2O_3 + 90%NMG (mixing 10 wt % pure Fe_2O_3 with 90 wt % NMG physically) is also given in Figure 7c, d, which exhibits much lower capacity at both 150 mA/g and 1000 mA/g than 10%Fe-NMG, confirming the structure integrity of the10%Fe-NMG during battery reactions. The gradual capacity

dx.doi.org/10.1021/am500323v | ACS Appl. Mater. Interfaces 2014, 6, 7189−7197

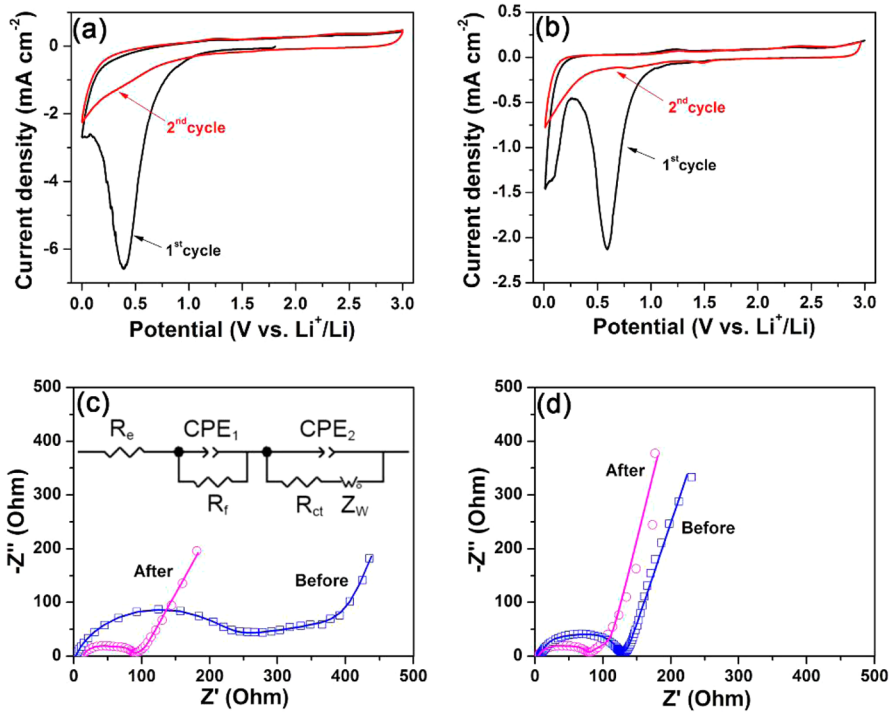

Figure 8. CV curves of (a) NMG and (b) 10%Fe-NMG composite at a scanning rate of 0.1 mV s^{-1}. AC impedance spectra of (c) NMG and (d) 10%Fe-NMG composite before and after charge/discharge cycles (the scatters represent raw data and the lines are fitting results).

increase observed for both NMG and 10%Fe-NMG is probably due to the gradual activation of porous graphene and Fe_2O_3 during the cycling process.[32] The excellent cycling performance of the 10%Fe-NMG composite is attributed to the good dispersion of Fe_2O_3 NPs on NMG, which efficiently prevents the aggregation of Fe_2O_3 NPs, thus maintaining the good cycling stability comparable to other iron-oxide-based anodes.[35−39] Although the 20%Fe-NMG composite have delivered a high Li storage capacity close to that of the 10%Fe-NMG composite in the first 30 cycles as shown in Figure 7b, the 20%Fe-NMG composite exhibits a downward trend during cycling at 150 mA g^{-1} (Figure 7c) and a delithiation capacity close to that of NMG at 1000 mA g^{-1} (Figure 7d). According to Figure 3d, a small amount of nanoparticles exhibit large particle size (20-30 nm) in the 20%Fe-NMG composite. It implies that large Fe_2O_3 particles are instable during cycling at a low current density and inefficient for Li storage at high rate. Due to the high content of Fe_2O_3 NPs in the 70%Fe-NMG composite (Figure 3e), the NMG could not provide enough surfaces to prohibit the agglomeration of Fe_2O_3 NPs, thus resulting in the poor cycling performance similar to the pure Fe_2O_3 electrode.

Compared to NMG, introduction of only ∼10 wt % Fe_2O_3 onto NMG has significantly promoted the Li storage capacity. As shown in Figure 7c, the final capacity for 10%Fe-NMG (1567 mA h g^{-1} at 150 mA g^{-1}) is 25.7% higher than that for NMG (1247 mA h g^{-1}). Considering that the theoretical capacity for Fe_2O_3 is 1005 mA h g^{-1}, the capacity contribution from Fe_2O_3 NPs should not be merely due to their reaction with lithium. CV curves for NMG and 10%Fe-NMG are shown in Figure 8a and b. In the first cycle for NMG, the broad cathodic peak at ∼0.4 V corresponds to lithium intercalation into the highly defective graphene layers of NMG. Compared to the cathodic peak at ∼0.4 V for NMG, the cathodic peak for the 10%Fe-NMG composite shifts to ∼0.6 V. The cathodic peaks at ∼0.8 and 1.5 V in the second cycle are only observed for 10%Fe-NMG (Figure 8b), corresponding to the two steps of the lithiation reactions of Fe_2O_3 (eq 1 and 2).[16,40]

$$Fe_2O_3 + 2Li^+ + 2e^- \rightarrow Li_2(Fe_2O_3) \quad (1)$$

$$Li_2(Fe_2O_3) + 4Li^+ + 4e^- \rightarrow 2Fe^0 + 3Li_2O \quad (2)$$

It indicates that the Fe_2O_3 NPs distributed on NMG are electroactive during the charge−discharge cycles. It is noticeable that the intensity of the broad cathodic peak at ∼0.4 V for NMG (6.6 mA cm^{-2}), corresponding to formation of SEI films, is much stronger than that for 10%Fe-NMG (0.9 mA cm^{-2}). It indicates that formation of SEI film on NMG might have been affected by the ultrasmall Fe_2O_3 NPs. Formation of SEI films on carbon is usually unavoidable, which involves an irreversible capacity loss. It has been reported that the SEI layers on carbon surface are much thicker than those on Co_3O_4 surface.[41,42] Therefore, the continuous growth of SEI films on the surface of NMG may be disturbed at the sites decorated by Fe_2O_3 NPs, and the Fe_2O_3 NPs may also catalyze the decomposition of SEI films on carbon surface, thus resulting in more reversible Li capacity during cycling.

AC impedance analysis provides further evidence to support the above speculation. The Nyquist plots of the AC impedance before and after charge/discharge cycles for NMG and 10%Fe-NMG are presented in panels c and d in Figure 8. The equivalent circuit shown in the inset of Figure 8c was used to fit the data points. In the circuit, R_e refers to the electrolyte resistance, R_f and CPE_1 are the resistance and capacitance (expressed by a constant phase element, CPE) of the surface film formed on the electrodes, R_{ct} and CPE_2 are the double-layer charge-transfer resistance and capacitance (expressed by a CPE), and Z_w is a generalized finite Warburg impedance related to the diffusion of lithium ions into the bulk of the electrodes. The calculated values of R_e, R_f, and R_{ct} through fitting of the experimental data are

summarized in Table 1. The high-frequency semicircle in Nyquist plots corresponds to the formation of SEI films and/or contact resistance.[5,43] The size of the high-frequency semicircle of 10%Fe-NMG is obviously smaller than that of NMG both before and after rate tests, indicating that there is a lower interfacial resistance and thinner SEI films in 10%Fe-NMG. The R_f value for 10%Fe-NMG before rate tests (49.5 Ω) is obviously smaller than the value for NMG (225.5 Ω), showing that the surface resistance has been significantly affected by the decoration of Fe_2O_3 NPs. The electrolyte resistance (R_e) of 10% Fe-NMG after charge−discharge cycles (4.1 Ω) is also lower than that of NMG (12.6 Ω), which might be also ascribed to the existence of Fe_2O_3 NPs in 10%Fe-NMG. The formation of thinner SEI films and smaller electrolyte resistance for 10%Fe-NMG provide clues showing the catalytic activity of Fe_2O_3 NPs for SEI film decomposition, thus significantly improving the lithium storage capacity and rate capability. This can be further confirmed by the high resolution TEM observation of 10%Fe-NMG after a sufficiently large number of discharge/charge cycles (Figure 9). As shown in Figure 9a, the outlines of the Fe_2O_3 NPs and NMG are blurred, which verifies the formation of SEI films. Columnar structures formed on the surface of Fe_2O_3 NPs are also observed in some view fields (Figure 9b), indicating that the formation and decomposition processes of SEI films with the existence of Fe_2O_3 NPs are quite different from those on the surface of NMG. The TEM image provides a powerful evidence to confirm our previous assumption that the Fe_2O_3 NPs may catalyze the decomposition of the SEI films.

Table 1. R_e, R_f, and R_{ct} Values of the NMG and 10%Fe-NMG Composite before and after Charge/Discharge Cycles

	NMG		10%Fe-NMG	
(Ω)	before	after	before	after
R_e	2.1	12.6	9.4	4.1
R_f	225.5	19.4	49.5	18.8
R_{ct}	137.7	51.5	61.0	50.7

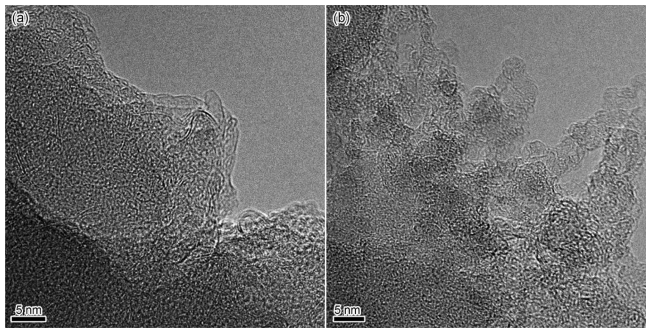

Figure 9. High-resolution TEM images of the 10%Fe-NMG after 50 discharge/charge cycles at the current density of 150 mA g^{-1}.

It has been reported that interfacial interaction can also contributed to the positive synergistic effect between graphene and metal oxides.[20,44] A careful comparison of XPS C 1s spectra of NMG and 10%Fe-NMG, before and after one charge−discharge cycle, is shown in Figure 10. In the C 1s spectrum of NMG (Figure 10a), the peaks at 284.2 and 285.2 eV can be attributed to graphitic carbon atoms with C═C and C−C bonds. In contrast, the peak at 289.1 eV, corresponding to C═O bonding configurations,[45] is observed in 10%Fe-NMG, indicating there is a strong interaction between Fe_2O_3 and NMG in the composite. In the C 1s spectra of NMG and 10%Fe-NMG after one charge−discharge cycle, peaks at 286.3, 289.0, and 290.0 eV, corresponding to C−O, C═O and O−C═O bonds, are observed (Figure 10c, d). The oxygen-containing functional groups should be ascribed to the formation of SEI films on surface. After the loading of Fe_2O_3 NPs, the intensity of the peaks corresponding to the oxygen-containing functional groups significantly deceases, which is a conclusive evidence showing that the Fe_2O_3 NPs can reduce the formation of SEI films on the carbon surface. On the whole, we give a thorough analysis of the catalytic role of the Fe_2O_3 NPs in the 10%Fe-NMG through the analysis of CV curves, TEM images, and XPS data after cycling.

Overall, the amazing lithium storage capacity and rate capability of the 10%Fe-NMG attribute to the following reasons. (i) The nanomesh structure of NMG acts as nanoscale vessels to load Fe_2O_3, offering an important platform for preparing the Fe_2O_3−NMG composite. The nanoscale vessels provide buffer for the expansion/shrinkage and recrystallization of Fe species. So the porous structure endows such composites with elastic deformation to retain the structure integrity during battery reactions. (ii) The NMG not only provide efficient diffusion channels for Li ions and a highly conductive pathway for electrons, but also provide more edges on sheet for the enhancement of Li ion storage. The lithium can be not only inserted in the NMG, but also attached on the walls of the mesopores and adsorbed on the surface of the NMG.[46,47] What's more, it can provide short ion diffusion lengths for low dimensional Fe_2O_3 nanoparticles to allow rapid ion transport. So the NMG contributes to the excellent rate capability and cycling stability for the composite. (iii) The Fe_2O_3 NPs distributed on NMG are electroactive during the charge−discharge cycles, which can affect the formation of SEI film on NMG and catalyze the decomposition of SEI films on carbon surface, thus resulting in more reversible Li capacity during cycling.

FeO_x−graphene composites have been reported by several groups.[48−51] In these reported FeO_x−graphene composites, the content of FeO_x is in the range of 20−90 wt %, and the diameter of FeO_x particles is in the range of 10−100 nm. Therefore, the FeO_x particles and graphene can separate each other to avoid agglomeration during cycling. In the Fe_2O_3 decorated NMG reported here, the ultrasmall Fe_2O_3 NPs are not used to separate graphene sheets since agglomeration of the NMG sheets has been avoided due to their surface corrugations and the Fe_2O_3 NPs are too small to separate graphene sheets. However, the metal oxide NPs work to change the surface condition of graphene, which is crucial to many applications. Our work provides a new insight into understanding the function of metal oxide NPs distributed on graphene sheets.

4. CONCLUSIONS

A Fe_2O_3−NMG composite that contains well-dispersed ultrasmall Fe_2O_3 NPs was synthesized by an adsorption−precipitation process. The reversible specific capacity of the 10%Fe-NMG composite reached 1567 mA h g^{-1} during 50 cycles at the current density of 150 mA g^{-1}, and 883 mA h g^{-1} during 100 cycles at 1000 mA g^{-1}, showing much enhanced capacity and rate capability. The cycling stability of the 10%Fe_2O_3−NMG composite was much better than those of 20% and 70%Fe_2O_3−NMG composite, because the porous structure of the composites could accommodate the large volume changes of Fe_2O_3. The significant capacity enhancement of the 10%Fe-NMG composite

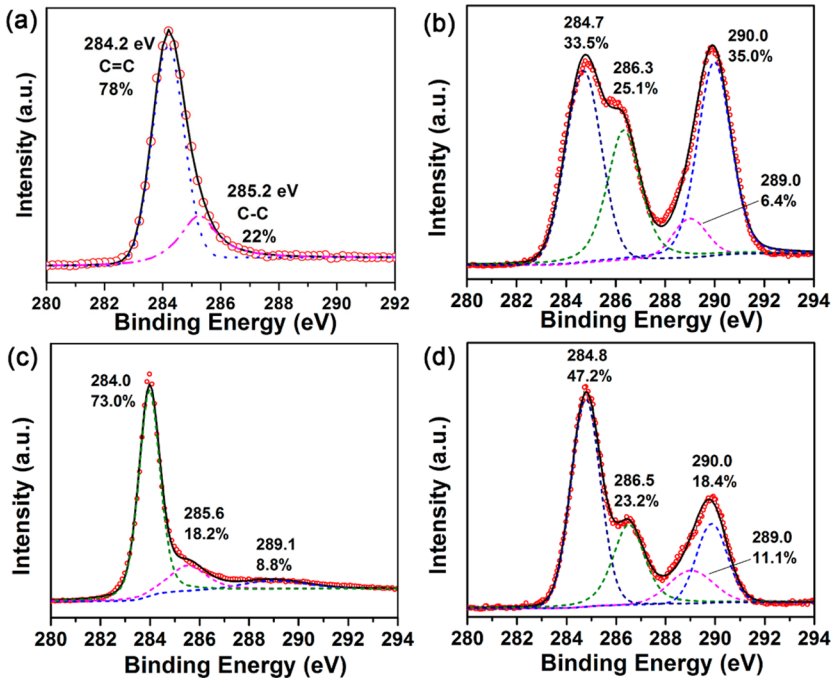

Figure 10. C 1s XPS spectra of the NMG (a) before and (b) after one cycle. C 1s XPS spectra of the 10%Fe-NMG (c) before and (d) after one cycle.

was attributed to the positive synergistic effect between NMG and Fe_2O_3 NPs because of the catalytic activity of Fe_2O_3 NPs for SEI film decomposition.

AUTHOR INFORMATION

Corresponding Author

*E-mail: ngq@cup.edu.cn.

Author Contributions

†Authors X.Z. and X.S. contributed equally.

Notes

The authors declare no competing financial interest.

ACKNOWLEDGMENTS

This work was supported by the National Natural Science Foundation of China (21206191).

REFERENCES

(1) Liu, J.; Cao, G.; Yang, Z.; Wang, D.; Dubois, D.; Zhou, X.; Graff, G. L.; Pederson, L. R.; Zhang, J. G. Oriented Nanostructures for Energy Conversion and Storage. *Chem. Sus. Chem.* **2008**, *1*, 676−697.

(2) Bruce, P. G.; Scrosati, B.; Tarascon, J. M. Nanomaterials for Rechargeable Lithium Batteries. *Angew. Chem., Int. Ed.* **2008**, *47*, 2930−2946.

(3) Ban, C.; Wu, Z.; Gillaspie, D. T.; Chen, L.; Yan, Y.; Blackburn, J. L.; Dillon, A. C. Nanostructured Fe_3O_4/SWNT Electrode: Binder-Free and High-Rate Li-Ion Anode. *Adv. Mater.* **2010**, *22*, E145−E149.

(4) Ke, F.-S.; Huang, L.; Solomon, B. C.; Wei, G.-Z.; Xue, L.-J.; Zhang, B.; Li, J.-T.; Zhou, X.-D.; Sun, S.-G. Three-Dimensional Nano-architecture of Sn-Sb-Co Alloy as an Anode of Lithium-Ion Batteries with Excellent Lithium Storage Performance. *J. Mater. Chem.* **2012**, *22*, 17511−17517.

(5) Jia, X.; Chen, Z.; Cui, X.; Peng, Y.; Wang, X.; Wang, G.; Wei, F.; Lu, Y. Building Robust Architectures of Carbon and Metal Oxide Nanocrystals toward High-Performance Anodes for Lithium-Ion Batteries. *ACS Nano* **2012**, *6*, 9911−9919.

(6) Zhang, H. X.; Feng, C.; Zhai, Y. C.; Jiang, K. L.; Li, Q. Q.; Fan, S. S. Cross-Stacked Carbon Nanotube Sheets Uniformly Loaded with SnO2 Nanoparticles: A Novel Binder-Free and High-Capacity Anode Material for Lithium-Ion Batteries. *Adv. Mater.* **2009**, *21*, 2299−2304.

(7) Wang, Z.; Zhou, L. Metal Oxide Hollow Nanostructures for Lithiu-Ion Batteries. *Adv. Mater.* **2012**, *24*, 1903−1911.

(8) Liu, X.-M.; Zhang, B.; Ma, P.-C.; Yuen, M. M.; Kim, J.-K. Carbon Nanotube (CNT)-based Composites as Electrode Material for Rechargeable Li-Ion Batteries: A Review. *Compos. Sci. Technol.* **2012**, *72*, 121−144.

(9) Mao, S.; Wen, Z.; Kim, H.; Lu, G.; Hurley, P.; Chen, J. A General Approach to One-Pot Fabrication of Crumpled Graphene-based Nanohybrids for Energy Applications. *ACS Nano* **2012**, *6*, 7505−7513.

(10) Latorre-Sanchez, M.; Primo, A.; Garcia, H. Green Synthesis of Fe3O4 Nanoparticles Embedded in a Porous Carbon Matrix and Its Use as Anode Material in Li-Ion Batteries. *J. Mater. Chem.* **2012**, *22*, 21373−21375.

(11) Muraliganth, T.; Murugan, A. V.; Manthiram, A. Facile Synthesis of Carbon-Decorated Single-Crystalline Fe3O4 Nanowires and Their Application as High Performance Anode in Lithium Ion Batteries. *Chem. Commun.* **2009**, 7360−7362.

(12) Jia, X.; Chen, Z.; Suwarnasarn, A.; Rice, L.; Wang, X.; Sohn, H.; Zhang, Q.; Wu, B. M.; Wei, F.; Lu, Y. High-Performance Flexible Lithium-Ion Electrodes Based on Robust Network Architecture. *Energy Environ. Sci.* **2012**, *5*, 6845−6849.

(13) Wang, H.; Liang, Y.; Gong, M.; Li, Y.; Chang, W.; Mefford, T.; Zhou, J.; Wang, J.; Regier, T.; Wei, F. An Ultrafast Nickel-Iron Battery from Strongly Coupled Inorganic Nanoparticle/Nanocarbon Hybrid Materials. *Nat. Commun.* **2012**, *3*, 917.

(14) Zhang, H.; Yu, X.; Braun, P. V. Three-Dimensional Bicontinuous Ultrafast-Charge and Discharge Bulk Battery Electrodes. *Nat. Nanotechnol.* **2011**, *6*, 277−281.

(15) Zhu, X.; Ning, G.; Ma, X.; Fan, Z.; Xu, C.; Gao, J.; Xu, C.; Wei, F. High Density Co3O4 Nanoparticles Confined in a Porous Graphene Nanomesh Network Driven by an Electrochemical Process: Ultra-High Capacity and Rate Performance for Lithium Ion Batteries. *J. Mater. Chem. A* **2013**, *1*, 14023−14030.

(16) Wang, J. Z.; Zhong, C.; Wexler, D.; Idris, N. H.; Wang, Z. X.; Chen, L. Q.; Liu, H. K. Graphene-Encapsulated Fe3O4 Nanoparticles with 3D Laminated Structure as Superior Anode in Lithium Ion Batteries. *Chem—Eur. J.* **2011**, *17*, 661−667.

(17) Wang, H.; Cui, L.-F.; Yang, Y.; Sanchez Casalongue, H.; Robinson, J. T.; Liang, Y.; Cui, Y.; Dai, H. Mn3O4−Graphene Hybrid as

a High-Capacity Anode Material for Lithium Ion Batteries. *J. Am. Chem. Soc.* **2010**, *132*, 13978−13980.
(18) Wu, Z. S.; Ren, W.; Wen, L.; Gao, L.; Zhao, J.; Chen, Z.; Zhou, G.; Li, F.; Cheng, H. M. Graphene Anchored with Co3O4 Nanoparticles as Anode of Lithium Ion Batteries with Enhanced Reversible Capacity and Cyclic Performance. *ACS Nano* **2010**, *4*, 3187−3194.
(19) Zhou, G.; Wang, D.-W.; Li, F.; Zhang, L.; Li, N.; Wu, Z.-S.; Wen, L.; Lu, G. Q.; Cheng, H.-M. Graphene-Wrapped Fe3O4 Anode Material with Improved Reversible Capacity and Cyclic Stability for Lithium Ion Batteries. *Chem. Mater.* **2010**, *22*, 5306−5313.
(20) Zhou, G.; Wang, D.-W.; Yin, L.-C.; Li, N.; Li, F.; Cheng, H.-M. Oxygen Bridges between NiO Nanosheets and Graphene for Improvement of Lithium Storage. *ACS Nano* **2012**, *6*, 3214−3223.
(21) Xin, S.; Guo, Y. G.; Wan, L. J. Nanocarbon Networks for Advanced Rechargeable Lithium Batteries. *J. Acc. Chem. Res.* **2012**, *45*, 1759−1769.
(22) Ning, G.; Fan, Z.; Wang, G.; Gao, J.; Qian, W.; Wei, F. Gram-Scale Synthesis of Nanomesh Graphene with High Surface Area and Its Application in Supercapacitor Electrodes. *Chem. Commun.* **2011**, *47*, 5976−5978.
(23) Zhu, X.; Zhu, Y.; Murali, S.; Stoller, M. D.; Ruoff, R. S. Nanostructured Reduced Graphene Oxide/Fe2O3 Composite as a High-Performance Anode Material for Lithium Ion Batteries. *ACS Nano* **2011**, *5*, 3333−3338.
(24) Stankovich, S.; Dikin, D. A.; Piner, R. D.; Kohlhaas, K. A.; Kleinhammes, A.; Jia, Y.; Wu, Y.; Nguyen, S. T.; Ruoff, R. S. Synthesis of Graphene-based Nanosheets via Chemical Reduction of Exfoliated Graphite Oxide. *Carbon* **2007**, *45*, 1558−1565.
(25) Guo, S.; Dong, S. Graphene Nanosheet: Synthesis, Molecular Engineering, Thin Film, Hybrids, and Energy and Analytical Applications. *Chem. Soc. Rev.* **2011**, *40*, 2644−2672.
(26) Ferrari, A.; Meyer, J.; Scardaci, V.; Casiraghi, C.; Lazzeri, M.; Mauri, F.; Piscanec, S.; Jiang, D.; Novoselov, K.; Roth, S. Raman Spectrum of Graphene and Graphene Layers. *Phys. Rev. Lett.* **2006**, *97*, 187401.
(27) Ago, H.; Imamura, S.; Okazaki, T.; Saito, T.; Yumura, M.; Tsuji, M. CVD Growth of Single-Walled Carbon Nanotubes with Narrow Diameter Distribution Over Fe/MgO Catalyst and Their Fluorescence Spectroscopy. *J. Phys. Chem. B* **2005**, *109*, 10035−10041.
(28) Ning, G.; Liu, Y.; Wei, F.; Wen, Q.; Luo, G. Porous and Lamella-Like Fe/MgO Catalysts Prepared under Hydrothermal Conditions for High-Yield Synthesis of Double-Walled Carbon Nanotubes. *J. Phys. Chem. C* **2007**, *111*, 1969−1975.
(29) Zhang, W. M.; Hu, J. S.; Guo, Y. G.; Zheng, S. F.; Zhong, L. S.; Song, W. G.; Wan, L. J. Tin-Nanoparticles Encapsulated in Elastic Hollow Carbon Spheres for High-Performance Anode Material in Lithium-Ion Batteries. *Adv. Mater.* **2008**, *20*, 1160−1165.
(30) Bhargava, G.; Gouzman, I.; Chun, C.; Ramanarayanan, T.; Bernasek, S. Characterization of the "Native" Surface Thin Film on Pure Polycrystalline Iron: A High Resolution XPS and TEM Study. *Appl. Surf. Sci.* **2007**, *253*, 4322−4329.
(31) He, X.; Ren, J.; Wang, L.; Pu, W.; Jiang, C.; Wan, C. Expansion and Shrinkage of the Sulfur Composite Electrode in Rechargeable Lithium Batteries. *J. Power Sources* **2009**, *190*, 154−156.
(32) Wang, Z.; Luan, D.; Madhavi, S.; Hu, Y.; Lou, X. W. D. Assembling Carbon-Coated α-Fe2O3 Hollow Nanohorns on the CNT Backbone for Superior Lithium Storage Capability. *Energy Environ. Sci.* **2012**, *5*, 5252−5256.
(33) Garcia-Belmonte, G.; García-Cañadas, J.; Bisquert, J. Correlation between Volume Change and Cell Voltage Variation with Composition for Lithium Intercalated Amorphous Films. *J. Phys. Chem. B* **2006**, *110*, 4514−4518.
(34) Kottegoda, I. R.; Idris, N. H.; Lu, L.; Wang, J.-Z.; Liu, H.-K. Synthesis and Characterization of Graphene−Nickel Oxide Nanostructures for Fast Charge−Discharge Application. *Electrochim. Acta* **2011**, *56*, 5815−5822.
(35) Ming, J.; Park, J.-B.; Sun, Y.-K. Encapsulation of Metal Oxide Nanocrystals into Porous Carbon with Ultrahigh Performances in Lithium-Ion Battery. *ACS Appl. Mater. Interfaces* **2013**, *5*, 2133−2136.
(36) Zhao, Y.; Li, J.; Ding, Y.; Guan, L. Single-Walled Carbon Nanohorns Coated with Fe2O3 as a Superior Anode Material for Lithium Ion Batteries. *Chem. Commun.* **2011**, *47*, 7416−7418.
(37) Reddy, M. V.; Subba Rao, G. V.; Chowdari, B. V. R. Metal Oxides and Oxysalts as Anode Materials for Li Ion Batteries. *Chem. Rev.* **2013**, *113*, 5364−5457.
(38) Chen, D.; Ji, G.; Ma, Y.; Lee, J. Y.; Lu, J. Graphene-Encapsulated Hollow Fe3O4 Nanoparticle Aggregates as a High-Performance Anode Material for Lithium Ion Batteries. *ACS Appl. Mater. Interfaces* **2011**, *3*, 3078−3083.
(39) Ji, L.; Toprakci, O.; Alcoutlabi, M.; Yao, Y.; Li, Y.; Zhang, S.; Guo, B.; Lin, Z.; Zhang, X. α-Fe2O3 Nanoparticle-Loaded Carbon Nanofibers as Stable and High-Capacity Anodes for Rechargeable Lithium-Ion Batteries. *ACS Appl. Mater. Interfaces* **2012**, *4*, 2672−2679.
(40) Zhu, J.; Zhu, T.; Zhou, X.; Zhang, Y.; Lou, X. W.; Chen, X.; Zhang, H.; Hng, H. H.; Yan, Q. Facile Synthesis of Metal Oxide/Reduced Graphene Oxide Hybrids with High Lithium Storage Capacity and Stable Cyclability. *Nanoscale* **2011**, *3*, 1084−1089.
(41) Laruelle, S.; Grugeon, S.; Poizot, P.; Dolle, M.; Dupont, L.; Tarascon, J. On the Origin of the Extra Electrochemical Capacity Displayed by MO/Li Cells at Low Potential. *J. Electrochem. Soc.* **2002**, *149*, A627−A634.
(42) Grugeon, S.; Laruelle, S.; Dupont, L.; Tarascon, J.-M. An Update on the Reactivity of Nanoparticles Co-based Compounds towards Li. *Solid State Sci.* **2003**, *5*, 895−904.
(43) Largeot, C.; Portet, C.; Chmiola, J.; Taberna, P.-L.; Gogotsi, Y.; Simon, P. Relation between the Ion Size and Pore Size for an Electric Double-Layer Capacitor. *J. Am. Chem. Soc.* **2008**, *130*, 2730−2731.
(44) Wu, Z.-S.; Zhou, G.; Yin, L.-C.; Ren, W.; Li, F.; Cheng, H.-M. Graphene/Metal Oxide Composite Electrode Materials for Energy Storage. *Nano Energy* **2012**, *1*, 107−131.
(45) Sheng, Z. H.; Shao, L.; Chen, J. J.; Bao, W. J.; Wang, F. B.; Xia, X. H. Catalyst-Free Synthesis of Nitrogen-Doped Graphene via Thermal Annealing Graphite Oxide with Melamine and Its Excellent Electrocatalysis. *ACS Nano* **2011**, *5*, 4350−4358.
(46) Fang, Y.; Lv, Y.; Che, R.; Wu, H.; Zhang, X.; Gu, D.; Zheng, G.; Zhao, D. Two-Dimensional Mesoporous Carbon Nanosheets and Their Derived Graphene Nanosheets: Synthesis and Efficient Lithium Ion Storage. *J. Am. Chem. Soc.* **2013**, *135*, 1524−1530.
(47) Fan, Z.; Yan, J.; Ning, G.; Wei, T.; Zhi, L.; Wei, F. Porous Graphene Networks as High Performance Anode Materials for Lithium Ion Batteries. *Carbon* **2013**, *60*, 558−561.
(48) Zhou, G. M.; Wang, D. W.; Li, F.; Zhang, L. L.; Li, N.; Wu, Z. S.; Wen, L.; Lu, G. Q.; Cheng, H. M. Graphene-Wrapped Fe3O4 Anode Material with Improved Reversible Capacity and Cyclic Stability for Lithium Ion Batteries. *Chem. Mater.* **2010**, *22*, 5306−5313.
(49) Wang, J. Z.; Zhong, C.; Wexler, D.; Idris, N. H.; Wang, Z. X.; Chen, L. Q.; Liu, H. K. Graphene-Encapsulated Fe3O4 Nanoparticles with 3D Laminated Structure as Superior Anode in Lithium Ion Batteries. *Chem.—Eur. J.* **2011**, *17*, 661−667.
(50) Wang, G.; Liu, T.; Luo, Y. J.; Zhao, Y.; Ren, Z. Y.; Bai, J. B.; Wang, H. Preparation of Fe2O3/Graphene Composite and Its Electrochemical Performance as an Anode Material for Lithium Ion Batteries. *J. Alloys Compd.* **2011**, *509*, L216−L220.
(51) Lian, P. C.; Zhu, X. F.; Xiang, H. F.; Li, Z.; Yang, W. S.; Wang, H. H. Enhanced Cycling Performance of Fe3O4-Graphene Composite as an Anode Material for Lithium-Ion Batteries. *Electrochim. Acta* **2010**, *56*, 834−840.